Supporting Information Appendix

High Capacity Rechargeable Batteries based on Deeply Cyclable Lithium Metal Anodes

Qiuwei Shi[1,2†], Yiren Zhong[1†], Min Wu[1†], Hongzhi Wang[2*], Hailiang Wang[1*]

[1]Department of Chemistry and Energy Sciences Institute, Yale University, 810 West Campus Drive, West Haven, CT 06516, USA.

[2]State Key Laboratory for Modification of Chemical Fibers and Polymer Materials, Donghua University, Shanghai 201620, P. R. China.

[†]These authors contributed equally

*E-mail: hailiang.wang@yale.edu; wanghz@dhu.edu.cn

Materials and methods

Preparation of $LiNO_3$-modified separators. A facile solution impregnation method was used to prepare $LiNO_3$-modified separators. 1 g of $LiNO_3$ was dissolved in 10 mL of 1, 2-dimethoxyethane (DME) to prepare a solution. Pristine glass fiber separators (15-mm diameter, Whatman) were soaked in the $LiNO_3$ solution for 2 h. The soaked separators were then taken out of the solution and fully dried in a vacuum antechamber of an Ar-filled glove box overnight at room temperature. The mass loading of $LiNO_3$ on a separator was weighed to be ~1 mg. Cycle life of Li||Cu cells is dependent on the mass loading of $LiNO_3$, and 1 mg appeared to give the best cyclability (Figure S24).

Synthesis of amorphous MoS_3. Multi-wall CNTs (CNano Technology) were first mildly oxidized via a modified Hummers' method as described in our previous report(1). Subsequently, 12 mg of oxidized CNTs were dispersed in 20 mL of deionized water under the assistance of sonication. The dispersion was then transferred to a 250 mL round bottom flask, to which was added 1 mmol of $(NH_4)_2MoS_4$ dissolved in 40 mL of deionized water, followed by addition of 1 M HCl (about 1 mL) till the solution pH was lowered to 3. The reaction mixture was stirred overnight. After reaction, the solid product was collected by centrifugation at 10000 rpm, washed with water, and lyophilized. Amorphous MoS_3 was finally obtained after annealing in an Ar atmosphere at 200 ^oC for 2 h.

Materials characterization. SEM imaging and EDX measurements were performed with a Hitachi SU8230 field emission SEM microscope. The dissembled electrodes subjected to later XPS

measurements were cleaned in an EC/DEC (1:1 volumetric ratio) solution and dried in an Ar-filled glove box. The samples were then transferred into the XPS chamber without exposure to air, using an air-tight vessel. The XPS spectra were obtained using monochromatic 1486.7 eV Al Kα X-ray source on a PHI VersaProbe II X-ray Photoelectron Spectrometer with a 0.47 eV system resolution. Depth profile measurements were carried out using Ar ion sputtering at the power of 0.5 kV x 7 mA (the first 6 min) and 5 kV x 7 mA (the following 60 min) over a 3 x 3 mm area. The estimated sputtering rates are 0.9 and 11.7 nm/min, respectively. XRD was performed with a Rigaku Smart Lab diffractometer with Cu K_α radiation.

Electrochemical measurement. For the Li||Cu cell measurements, 2032-type coin cells were assembled with a pristine or $LiNO_3$-modified glass fiber separator, a 13 mm-diameter Li foil disk (450 μm in thickness) and a 14 mm-diameter Cu foil disk. Electrochemical Li plating at a certain current density was performed until a certain capacity was reached, followed by Li stripping at the same current density with a cut-off voltage of 0.5 V. For the Li||Li cell measurements, symmetric cells were assembled with a 13 mm-diameter Li foil disks as both the working and counter electrodes. Long-term galvanostatic cycling was then performed at a certain current density with a certain cut-off capacity. To prepare the MoS_3 cathode, a slurry containing MoS_3-CNT, carbon black and polyvinylidene difluoride in the mass ratio of 75:15:10 was casted onto a 10 mm-diameter carbon paper (Spectracarb 2050A-0550, Fuel Cell Store) disk to give an areal mass loading of ~12 mg cm^{-2} (based on MoS_3-CNT). For all the cells, a 1 M $LiPF_6$-EC/DEC (1:1 volumetric ratio) electrolyte (BASF) was used as received. The cells were measured by a BT2143 battery analyzer (Arbin Instrument). The EIS measurements were carried out using a Biologic VMP3 multichannel system.

Supporting Figures

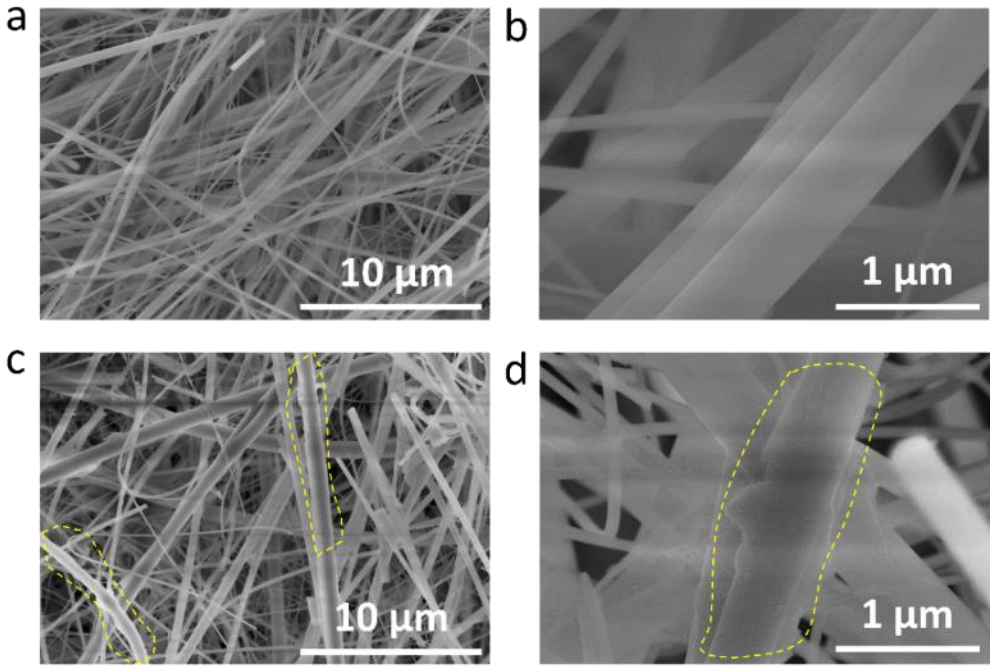

Figure S1. SEM images of pristine (a, b) and $LiNO_3$-modified (c, d) glass fiber separators at different magnifications.

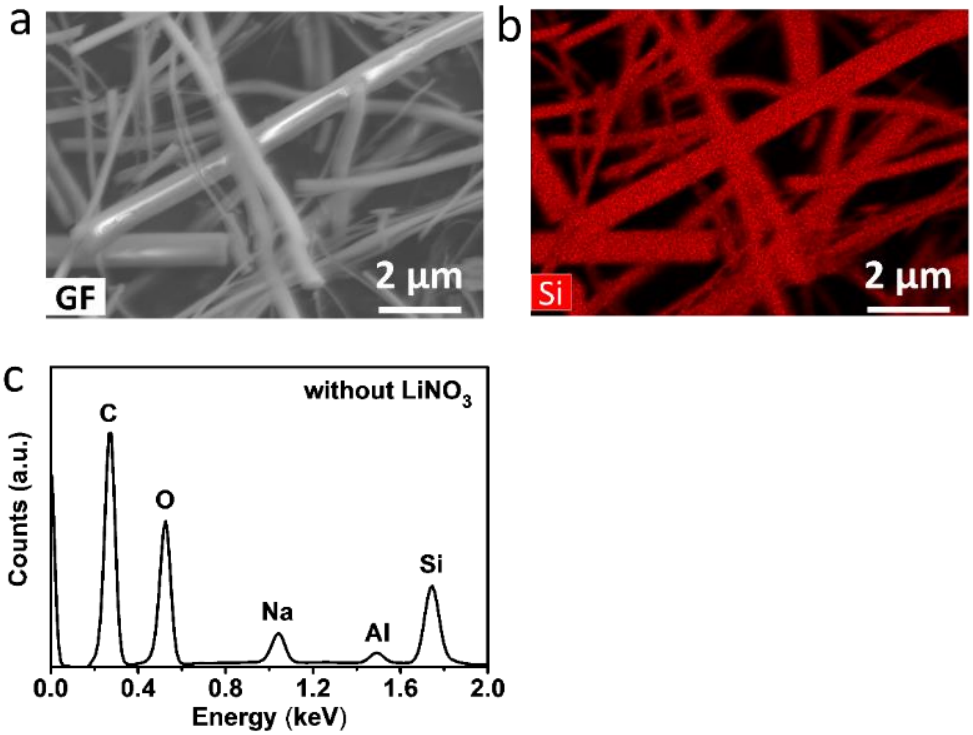

Figure S2. SEM-EDX analysis of the pristine glass fiber separator. (a) SEM image; (b) elemental distribution map of Si; (c) the corresponding EDX spectrum.

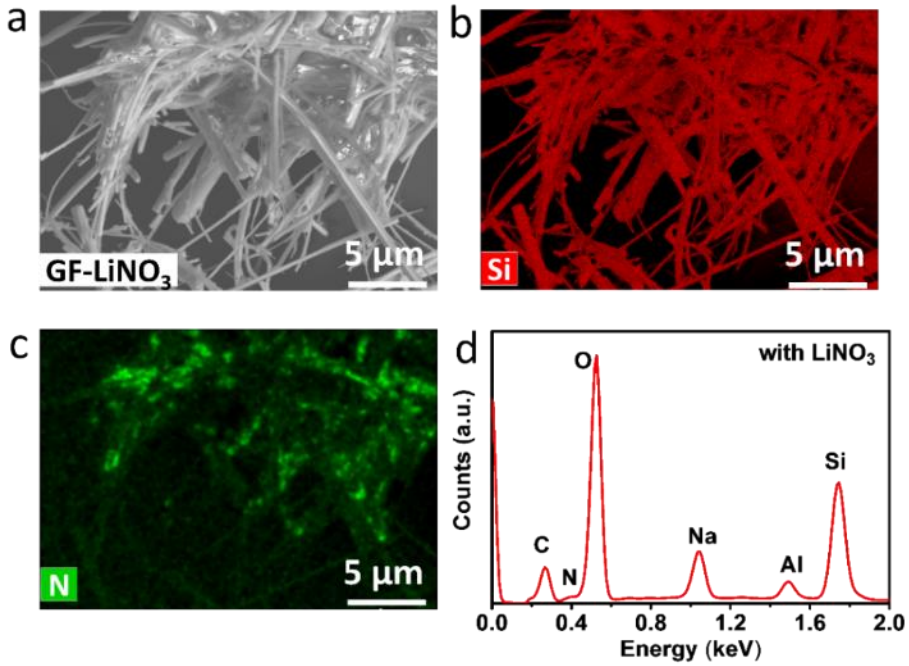

Figure S3. SEM-EDX analysis of the $LiNO_3$-modified separator. (a) SEM image; (b, c) elemental distribution maps of Si and N; (d) the corresponding EDX spectrum.

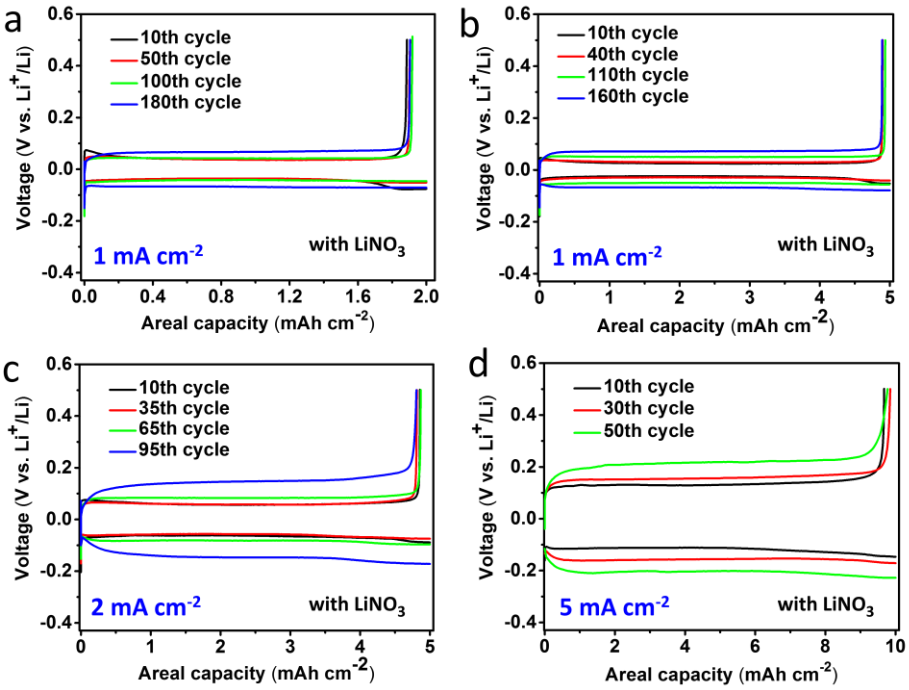

Figure S4. Discharging and charging voltage profiles of Li||Cu cells with $LiNO_3$ measured under various current-capacity conditions.

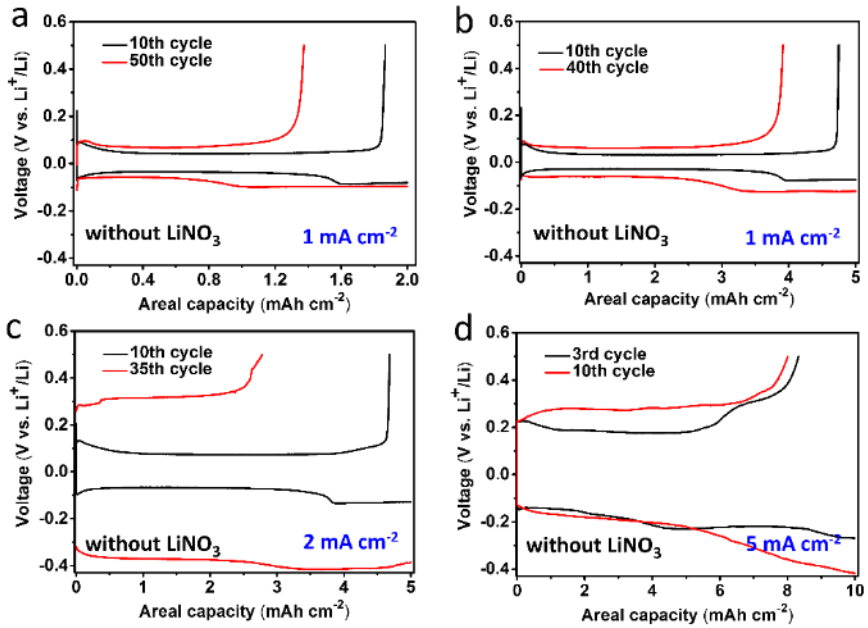

Figure S5. Discharging and charging voltage profiles of Li||Cu cells measured under various current-capacity conditions.

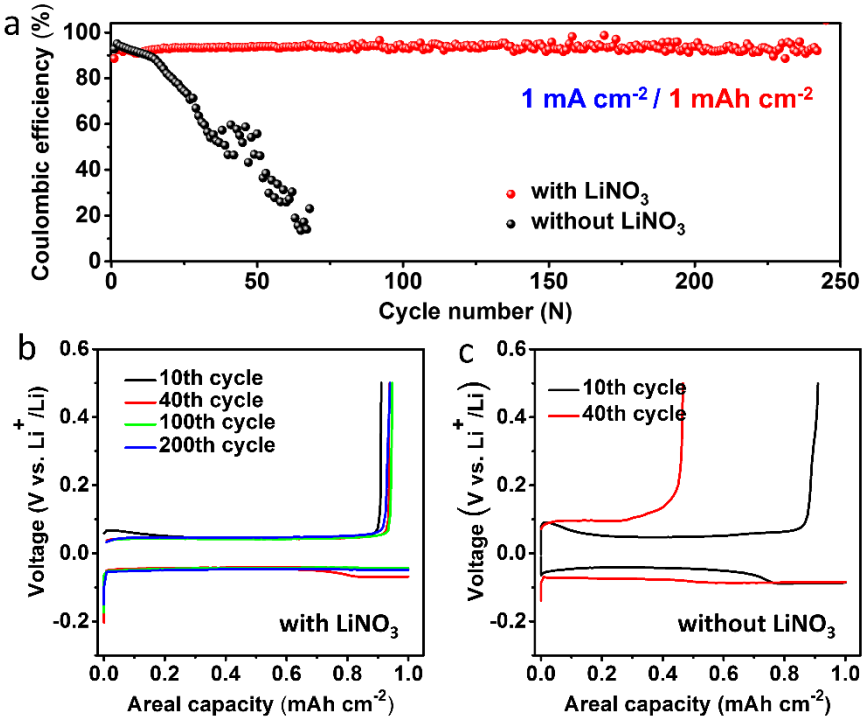

Figure S6. (a) CE of Li||Cu cells with and without $LiNO_3$ under 1 mA cm^{-2}–1 mAh cm^{-2} conditions. (b, c) The corresponding discharging and charging voltage profiles.

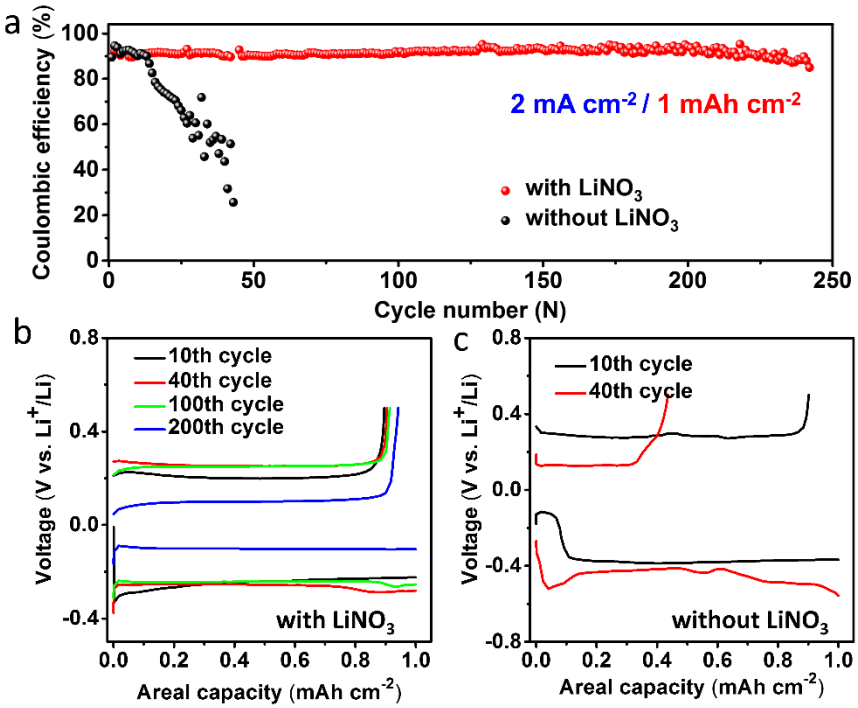

Figure S7. (a) CE of Li||Cu cells with and without $LiNO_3$ under 2 mA cm^{-2}–1 mAh cm^{-2} conditions. (b, c) The corresponding discharging and charging voltage profiles.

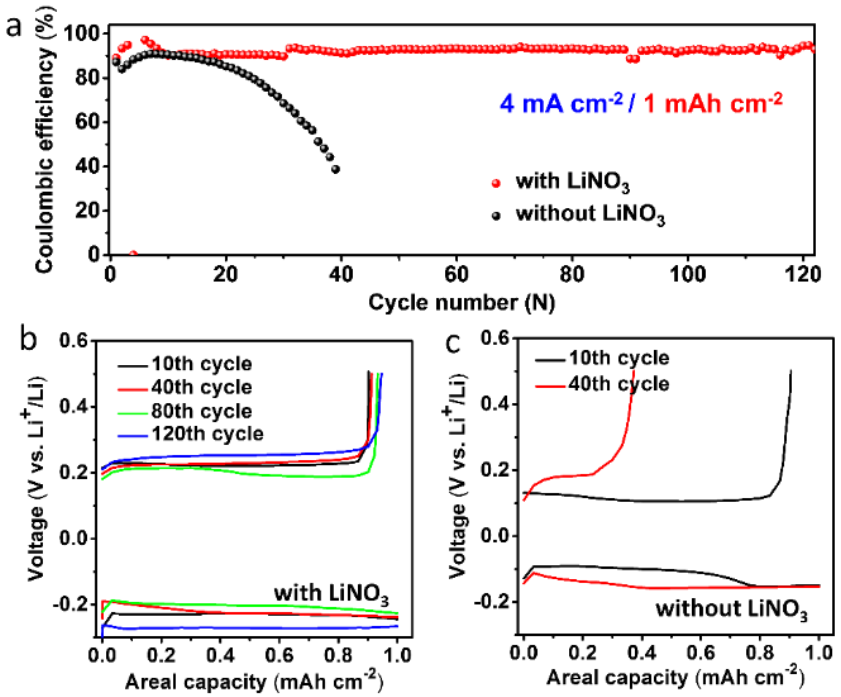

Figure S8. (a) CE of Li||Cu cells with and without $LiNO_3$ under 4 mA cm^{-2}–1 mAh cm^{-2} conditions. (b, c) The corresponding discharging and charging voltage profiles.

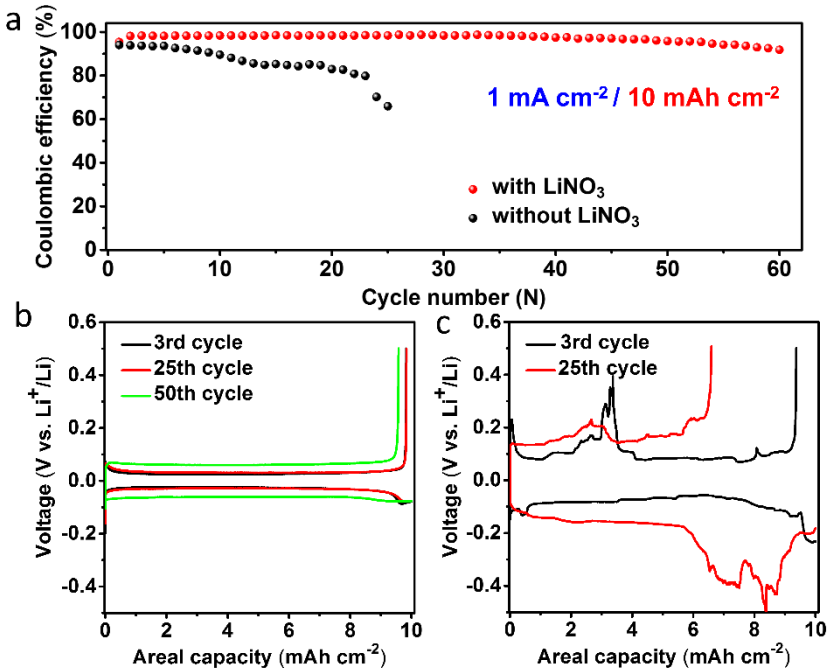

Figure S9. (a) CE of Li||Cu cells with and without $LiNO_3$ under 1 mA cm^{-2}–10 mAh cm^{-2} conditions. (b, c) The corresponding discharging and charging voltage profiles.

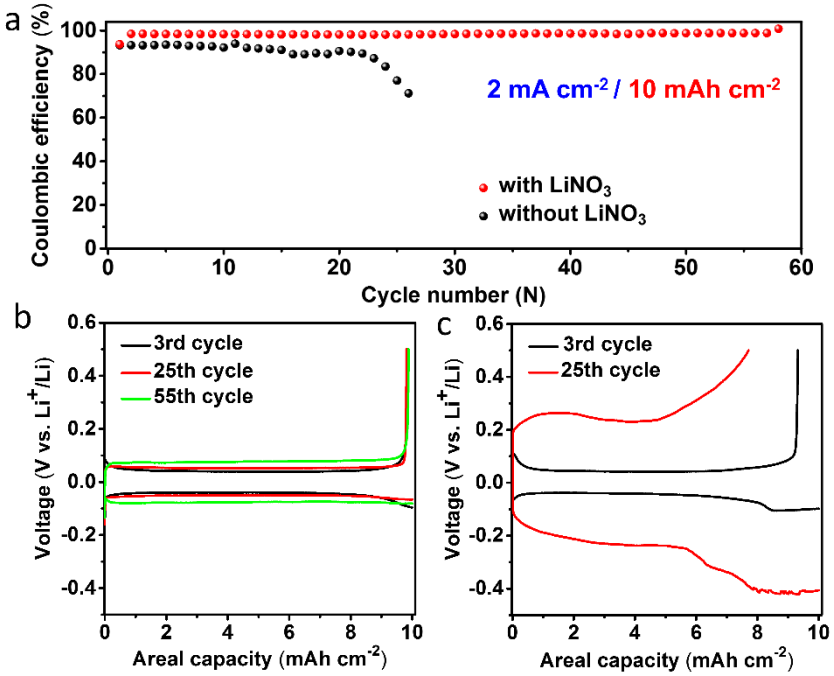

Figure S10. (a) CE of Li||Cu cells with and without $LiNO_3$ under 2 mA cm^{-2}–10 mAh cm^{-2} conditions. (b, c) The corresponding discharging and charging voltage profiles.

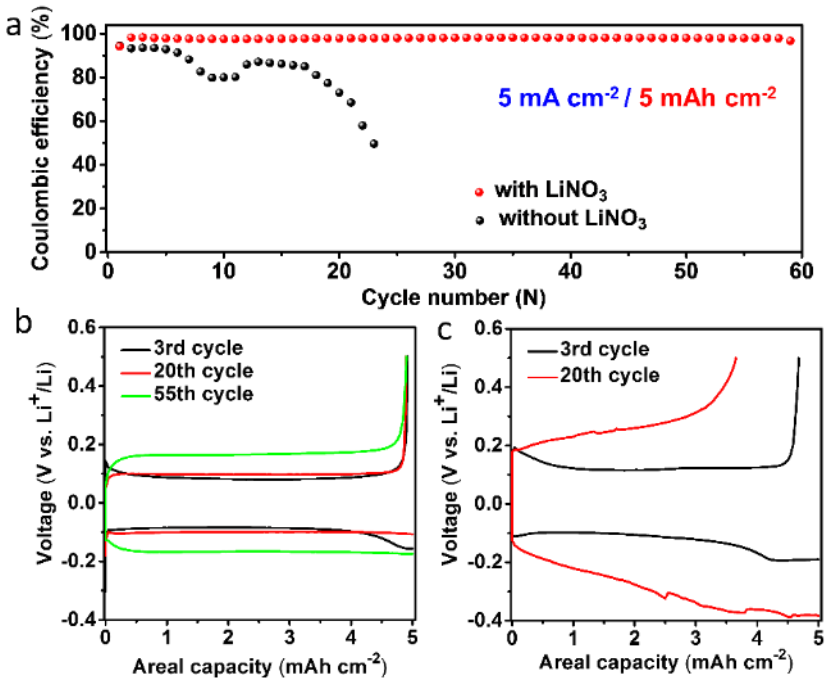

Figure S11. (a) CE of Li||Cu cells with and without $LiNO_3$ under 5 mA cm^{-2}–5 mAh cm^{-2} conditions. (b, c) The corresponding discharging and charging voltage profiles.

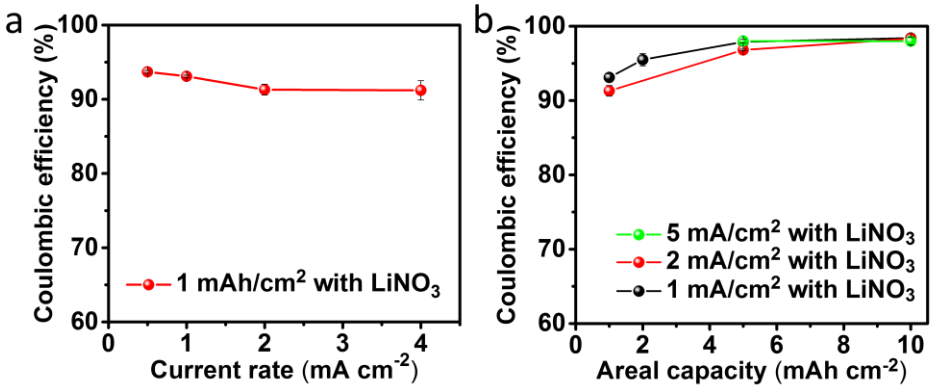

Figure S12. Dependence of CE on current and capacity for Li||Cu cells with $LiNO_3$. (a) Dependence of CE on current density at a fixed cycling capacity of 1 mAh cm^{-2}. (b) Dependence of CE on capacity at various current densities.

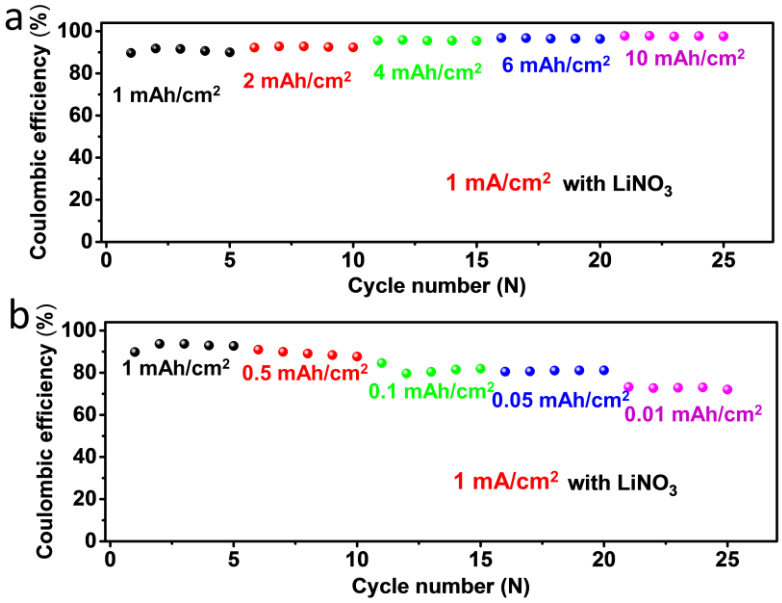

Figure S13. CE of Li||Cu cells with $LiNO_3$ cycled at a fixed current density of 1 mA cm^{-2} with the charging/discharging capacity (a) increased and (b) decreased stepwise.

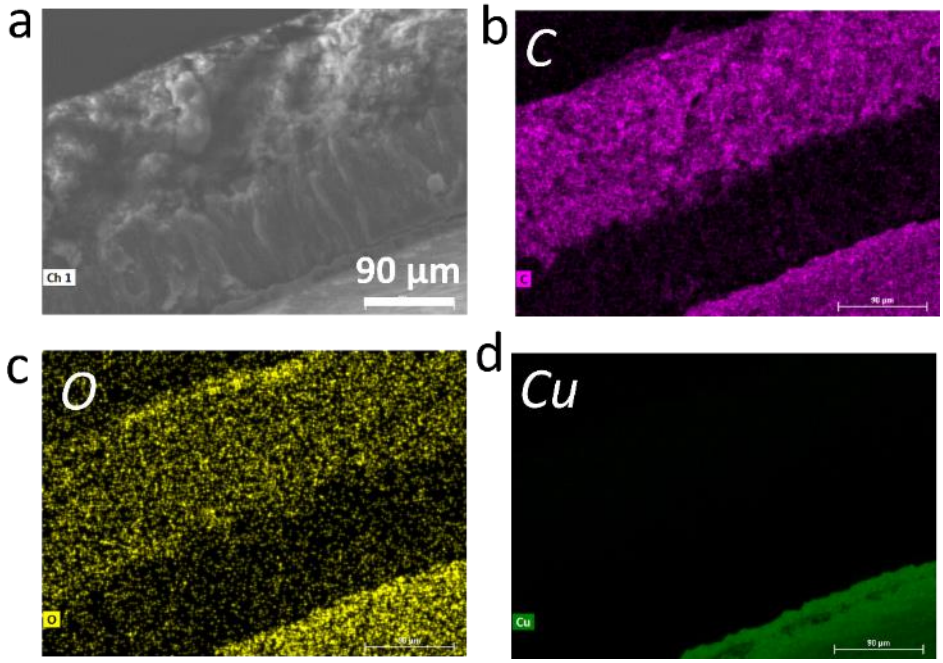

Figure S14. SEM-EDX analysis of the Li plated on the Cu foil for a Li||Cu cell without $LiNO_3$ after 20 cycles under 2 mA cm^{-2}–10 mAh cm^{-2} conditions. (a) SEM image; (b-d) elemental distribution maps of C, O and Cu.

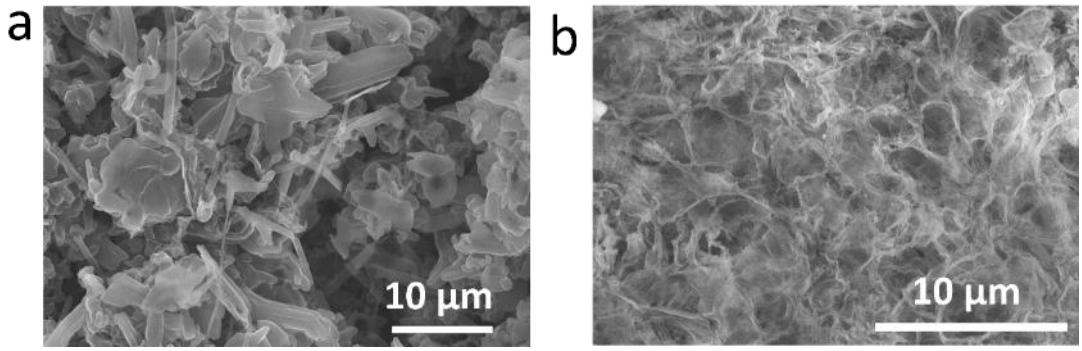

Figure S15. Top-view SEM images of the Li plated on the Cu foil after 3 cycles under 2 mA cm^{-2}–10 mAh cm^{-2} conditions for Li||Cu cells (a) without and (b) with $LiNO_3$.

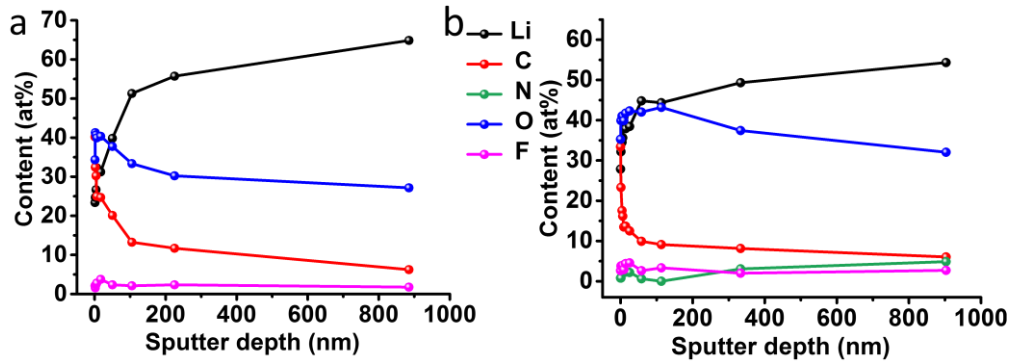

Figure S16. XPS depth profiles of the plated Li layer on the Cu foil after 3 cycles under 2 mA cm^{-2}–10 mAh cm^{-2} conditions for Li||Cu cells (a) without and (b) with $LiNO_3$.

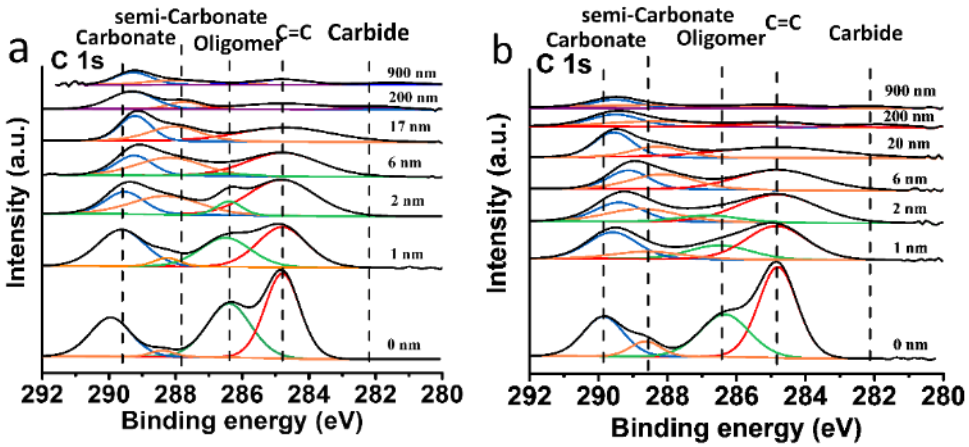

Figure S17. C 1s XPS spectra at various depths of the plated Li layer on the Cu foil after 3 cycles under 2 mA cm^{-2}–10 mAh cm^{-2} conditions for Li||Cu cells (a) without and (b) with $LiNO_3$.

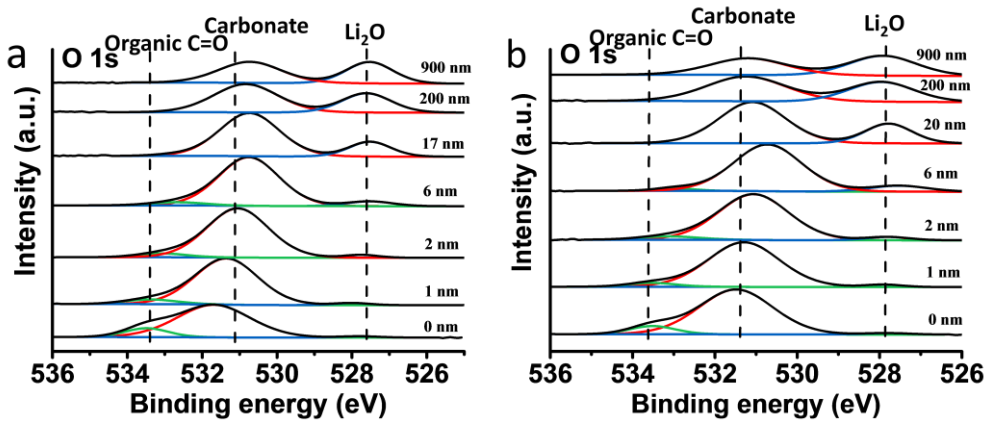

Figure S18. O 1s XPS spectra at various depths of the plated Li layer on the Cu foil after 3 cycles under 2 mA cm^{-2}–10 mAh cm^{-2} conditions for Li||Cu cells (a) without and (b) with $LiNO_3$.

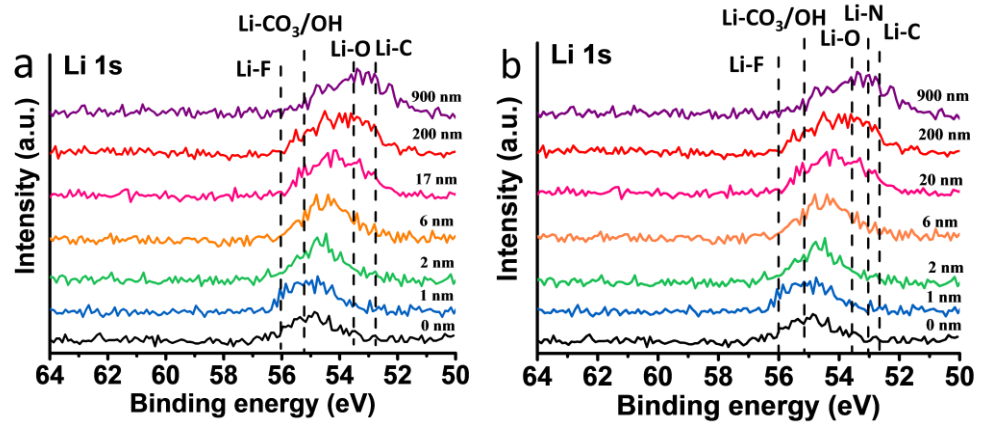

Figure S19. Li 1s XPS spectra at various depths of the plated Li layer on the Cu foil after 3 cycles under 2 mA cm^{-2}–10 mAh cm^{-2} conditions for Li||Cu cells (a) without and (b) with $LiNO_3$.

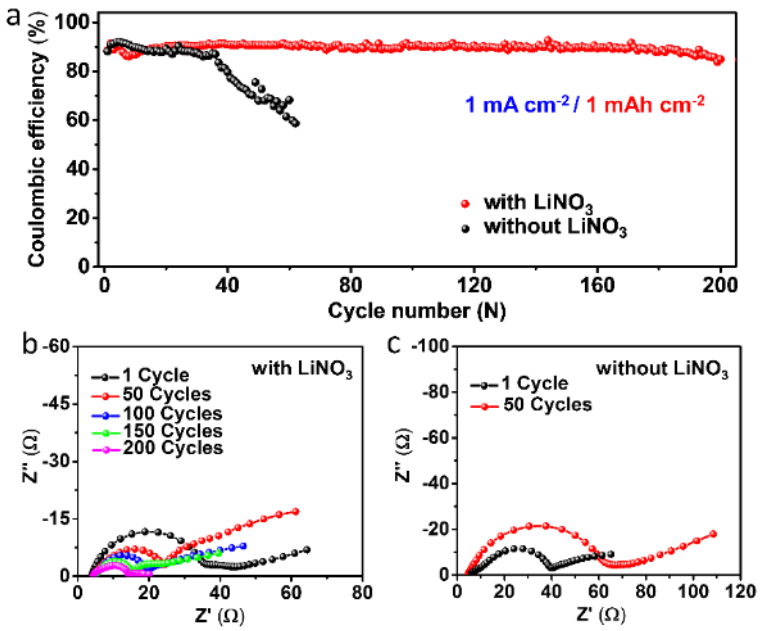

Figure S20. (a) CE of Li||Cu cells with and without $LiNO_3$ cycled under 1 mA cm^{-2}–1 mAh cm^{-2} conditions. (b, c) The corresponding EIS spectra (frequency range of 300 kHz to 10 mHz) taken at the full Li-plated state (1 mAh cm^{-2} of Li plated on the Cu foil) after various numbers of cycles.

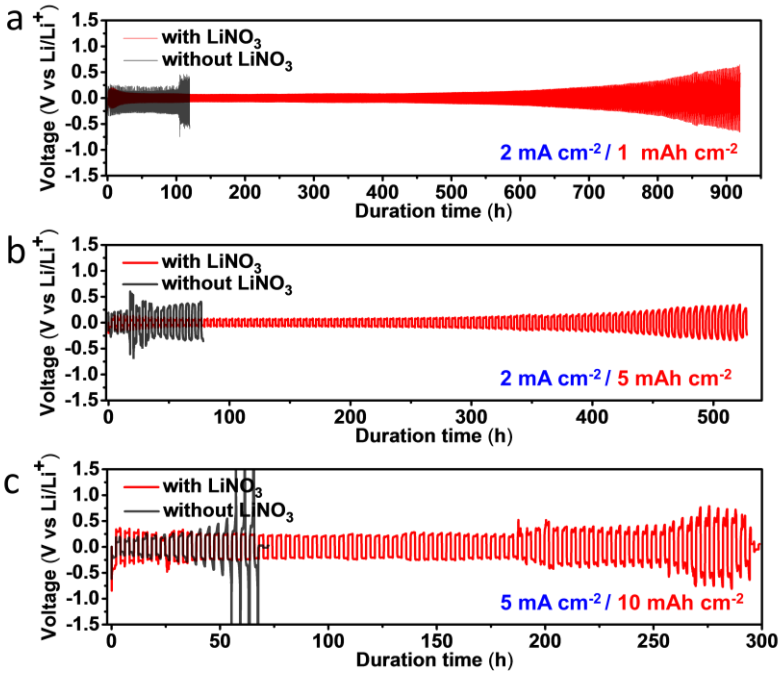

Figure S21. Cycling performance of Li||Li symmetric cells with and without $LiNO_3$ under (a) 2 mA cm^{-2}–1 mAh cm^{-2}, (b) 2 mA cm^{-2}–5 mAh cm^{-2}, and (c) 5 mA cm^{-2}–10 mAh cm^{-2} conditions.

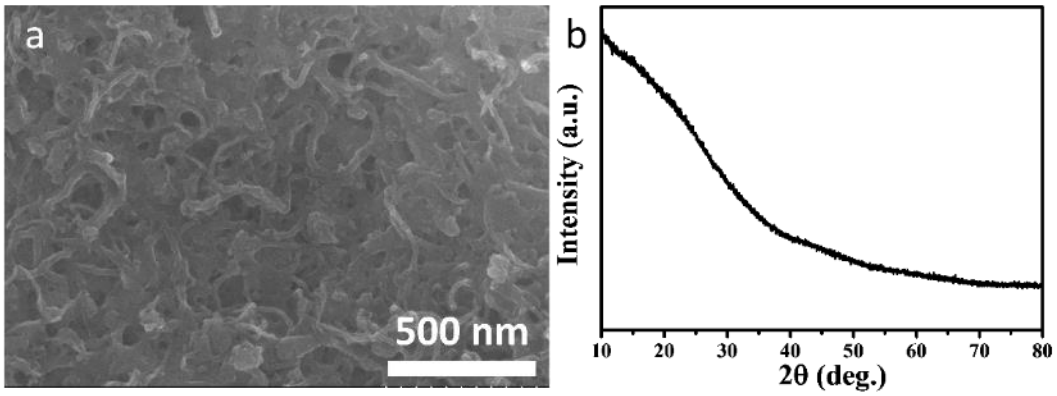

Figure S22. (a) SEM image and (b) XRD pattern of MoS_3-CNT.

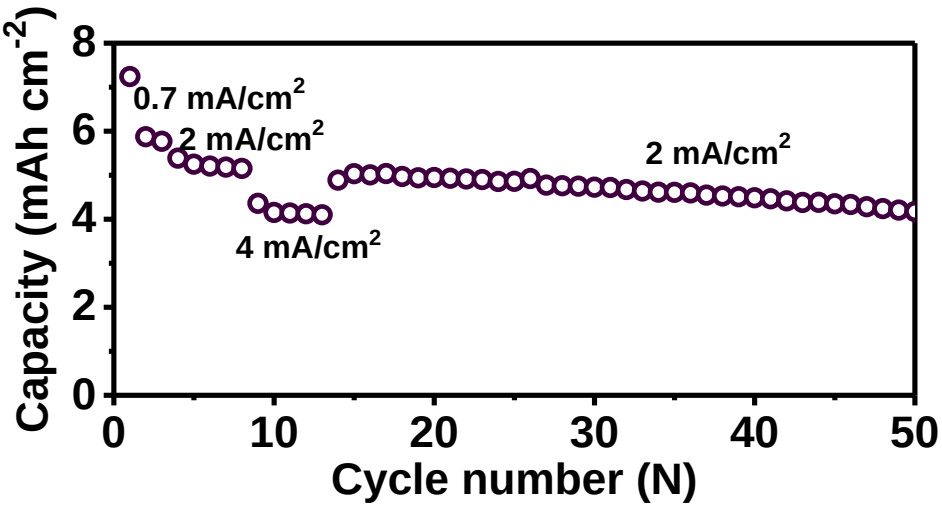

Figure S23. Electrochemical performance of a MoS_3-CNT cathode measured against a Li foil.

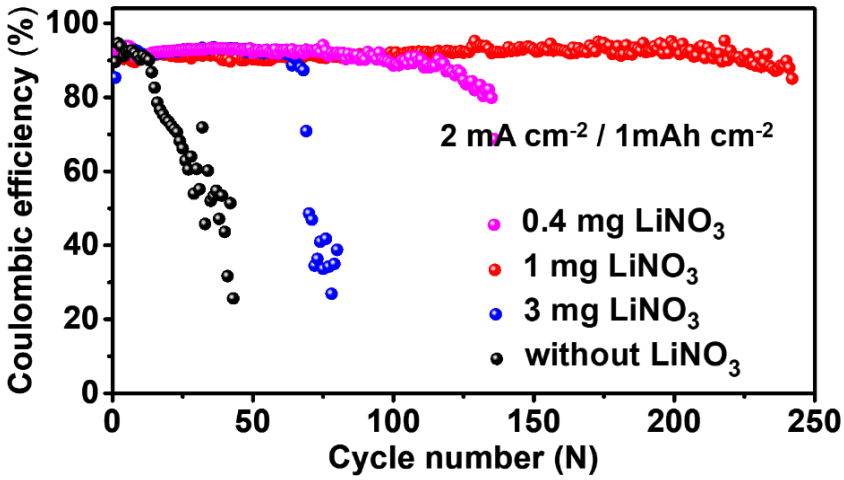

Figure S24. CE of Li||Cu cells with different mass loadings of $LiNO_3$ in the separator cycled under 2 mA cm^{-2}–1 mAh cm^{-2} conditions.

Supporting Tables

Table S1. Electrochemical performance of the $LiNO_3$-protected Li electrodes in Li||Cu cells compared with available data in the literature.

Method	Current ($mA\ cm^{-2}$)	Capacity ($mAh\ cm^{-2}$)	Cycles	CE	Ref.
$LiNO_3$-protected, 1 M $LiPF_6$ (EC:DEC)	1	1	242	92.2%	This work
	2	1	240	93.7%	
	4	1	120	92.7%	
	1	2	217	95.1%	
	1	5	160	98.3%	
	1	10	60	98.4%	
	2	5	100	96.8%	
	5	5	59	98.0%	
	2	10	57	98.5%	
	5	10	53	98.1%	
Lithium in 3D nickel foam host (1 M $LiPF_6$, EC:DEC:EMC=1:1:1)	1	1	100	86%	(2)
1 M $LiPF_6$ (EC:DMC) with 0.5 wt% LiF additive	0.25	1	120	89%	(3)
	0.5	1	120	87%	
SiO_2@PMMA core@shell nanospheres on Cu foil, 1 M $LiPF_6$ (EC:DMC)	1	2	50	90%	(4)
	0.5	2	50	83%	
Polyimide coating layer with vertical nanoscale channels, 1 M $LiPF_6$ (EC:DEC)	1	1	40	89%	(5)
Cu_3N and styrene butadiene rubber (1 M LiPF6 EC/DEC with 10 wt% FEC additive)	1	1	100	97%	(6)
	0.25	0.5	150	98%	
Cu nanowire network (1 M LiPF6 EC/DMC with VC additive)	1	1	50	93%	(7)

BN coated on separator, 1 M LiPF6 (EC:DEC)	0.25	1	100	94%	(8)
	0.5	1	100	92%	
	1	1	100	88%	
h-BN on Cu foil, 1 M LiPF6 EC/DEC	1	1	50	93%	(9)
	1	3	50	95%	
	1	5	50	95%	
1 M $LiPF_6$ (EC/DMC/DEC, 1:1:1) with $AlCl_3$ additive	0.5	2	150	98%	(10)
1 M $LiPF_6$ (EC/DEC) with 5 vol.% FEC additive	0.1	0.5	100	98%	(11)
	0.5	0.5	100	95%	
Poly(dimethylsiloxane) artificial SEI and 1 M $LiPF_6$ (EC/DEC) with 2 wt% VC additive	0.25	1	200	93%	(12)
	0.5	1	100	90%	
	1	1	100	89%	
Carbon-based 3D current collector, 1 M $LiPF_6$ (EC/DEC)	1	2	80	92%	(13)
3D hierarchical porous carbon with ZnO quantum dots, 1 M $LiPF_6$ (EC/DMC) with 1 wt% FEC additive	0.5	1	80	90%	(14)
Hollow carbon spheres with gold nanoparticle seeds inside, 1 M $LiPF_6$ (EC/DEC) with 1% VC and 10% FEC additives	0.5	1	300	98%	(15)
3D Cu-Ni core-shell nanowire network, 1 M $LiPF_6$ (EC/DEC)	2	2	100	92%	(16)
Lithium-fluoride protected Cu current collectors, 1 M $LiPF_6$ (EC/DEC)	0.5	1	140	85%	(17)
Coating Li metal surface with a polymer layer, 1M $LiPF_6$ (EC:EMC:FEC=3:7:1)	0.5	1	200	98%	(18)

Table S2. Electrochemical performance of the $LiNO_3$-protected Li electrodes in Li||Li cells compared with available data in the literature.

Method	Current ($mA\ cm^{-2}$)	Capacity ($mAh\ cm^{-2}$)	Time (hour)	Ref.
$LiNO_3$-protected, 1 M $LiPF_6$ (EC:DEC)	1	1	1420	This work
	2	1	930	
	2	2	690	
	2	5	530	
	5	5	423	
	5	10	290	
	5	20	180	
Lithium in 3D nickel foam host (1 M $LiPF_6$, EC:DEC:EMC=1:1:1)	1	1	210	(2)
	3	1	70	
	5	1	40	
1 M $LiPF_6$ (EC:DEC) with 0.5 wt% LiF additive	1	4	1700	(3)
	2	4	580	
	4	4	140	
1 M $LiPF_6$ (EC/DMC/DEC, 1:1:1) with $AlCl_3$ additive	0.5	2	940	(10)
Carbon-based 3D current collector, 1 M $LiPF_6$ (EC/DEC)	1	1	45	(13)
	3	1	60	
3D hierarchical porous carbon with ZnO quantum dots, 1 M $LiPF_6$ (EC/DEC) with 1 wt% FEC additive	0.5	1	500	(14)
Al_2O_3-coated Li, 1 M $LiPF_6$ (EC:EMC)	1	1	240	(19)
Lithium infused in a 3D porous carbon matrix with Si coating, 1 M $LiPF_6$ (EC:DEC)	3	1	70	(20)
Infusing Li into the channel structure of C-wood, 1 M $LiPF_6$ (EC:DEC)	0.5	1	850	(21)
	1	1	350	
	3	1	155	

Layered Li–rGO composite, 1 M $LiPF_6$ (EC:DEC) with 2% VC additive	1	1	225	(22)
	3	1	70	
Li deposited on core-shell polyimide-ZnO matrix, 1 M $LiPF_6$ (EC:DEC)	1	1	195	(23)
	3	1	67	
	5	1	40	
Dry N_2-passivated Li metal anodes, 1 M $LiPF_6$ (EC:DEC)	1	1	333	(24)
1 M $LiPF_6$ (EC:DEC) with 10 mM KPF_6 additive	0.5	0.5	210	(25)
Poly(ethyl α‑cyanoacrylate) based artificial SEI on Li metal, 1 M $LiPF_6$ (EC:DEC)	1	1	400	(26)
LiF-coated layered Li-rGO electrodes, 1 M $LiPF_6$ (EC:DEC) with 10% FEC and 1% VC additives	1	1	450	(27)
Li_3N-modified Li electrode, 1 M $LiPF_6$ (EC:DEC)	1	2	360	(28)
In-situ formed Li_xM (In, Zn, As) alloy films on Li metal, 1 M $LiPF_6$ (EC:DMC)	2	2	400	(29)
1 M $LiPF_6$ (EC:DMC) with nano-diamond additive,	1	0.2	200	(30)
	2	0.4	150	
Mesoporous AlF_3 framework, 1 M $LiPF_6$ (EC:DEC) with 10% FEC and 1% VC additives	1	1	194	(31)
	10	1	194	
	20	1	9.7	
Coating Li metal surface with a polymer layer, 1M $LiPF_6$ (EC:EMC:FEC=3:7:1)	0.5	1	300	(18)

Supporting References

1. Liu W*, et al.* (2016) A highly active and stable hydrogen evolution catalyst based on pyrite-structured cobalt phosphosulfide. *Nat Commun* 7:10771.
2. Chi S-S, Liu Y, Song W-L, Fan L-Z, & Zhang Q (2017) Prestoring Lithium into Stable 3D Nickel Foam Host as Dendrite-Free Lithium Metal Anode. *Adv Funct Mater* 27(24):1700348.
3. Choudhury S & Archer LA (2016) Lithium Fluoride Additives for Stable Cycling of Lithium Batteries at High Current Densities. *Adv Electron Mater* 2(2):1500246.
4. Liu W*, et al.* (2017) Core-Shell Nanoparticle Coating as an Interfacial Layer for Dendrite-Free Lithium Metal Anodes. *ACS Cent Sci* 3(2):135-140.
5. Liu W, Lin D, Pei A, & Cui Y (2016) Stabilizing Lithium Metal Anodes by Uniform Li-Ion Flux Distribution in Nanochannel Confinement. *J Am Chem Soc* 138(47):15443-15450.
6. Liu Y*, et al.* (2017) An Artificial Solid Electrolyte Interphase with High Li-Ion Conductivity, Mechanical Strength, and Flexibility for Stable Lithium Metal Anodes. *Adv Mater* 29(10):1605531.
7. Lu LL*, et al.* (2016) Free-Standing Copper Nanowire Network Current Collector for Improving Lithium Anode Performance. *Nano Lett* 16(7):4431-4437.
8. Luo W*, et al.* (2015) A Thermally Conductive Separator for Stable Li Metal Anodes. *Nano Lett* 15(9):6149-6154.
9. Yan K*, et al.* (2014) Ultrathin Two-Dimensional Atomic Crystals as Stable Interfacial Layer for Improvement of Lithium Metal Anode. *Nano Lett* 14(10):6016-6022.
10. Ye H*, et al.* (2017) Synergism of Al-containing solid electrolyte interphase layer and Al-based colloidal particles for stable lithium anode. *Nano Energy* 36:411-417.
11. Zhang X-Q, Cheng X-B, Chen X, Yan C, & Zhang Q (2017) Fluoroethylene Carbonate Additives to Render Uniform Li Deposits in Lithium Metal Batteries. *Adv Funct Mater* 27(10):1605989.
12. Zhu B*, et al.* (2017) Poly(dimethylsiloxane) Thin Film as a Stable Interfacial Layer for High-Performance Lithium-Metal Battery Anodes. *Adv Mater* 29(2):1603755.
13. Zhang Y*, et al.* (2017) A carbon-based 3D current collector with surface protection for Li metal anode. *Nano Research* 10(4):1356-1365.
14. Jin C*, et al.* (2017) 3D lithium metal embedded within lithiophilic porous matrix for stable lithium metal batteries. *Nano Energy* 37:177-186.
15. Yan K*, et al.* (2016) Selective deposition and stable encapsulation of lithium through heterogeneous seeded growth. *Nat Energy* 1(3):16010.
16. Lu L-L*, et al.* (2017) Lithiophilic Cu–Ni core–shell nanowire network as a stable host for improving lithium anode performance. *Energy Storage Mater* 9:31-38.
17. Zhang XQ*, et al.* (2017) Columnar Lithium Metal Anodes. *Angew Chem Int Ed Engl* 56(45):14207-14211.
18. Gao Y*, et al.* (2017) Interfacial Chemistry Regulation via a Skin-Grafting Strategy Enables High-Performance Lithium-Metal Batteries. *J Am Chem Soc* 139(43):15288-15291.
19. Chen L*, et al.* (2017) Lithium metal protected by atomic layer deposition metal oxide for high performance anodes. *J. Mater. Chem. A* 5(24):12297-12309.
20. Liang Z*, et al.* (2016) Composite lithium metal anode by melt infusion of lithium into a 3D conducting scaffold with lithiophilic coating. *Proceedings of the National Academy of Sciences* 113(11):2862-2867.
21. Zhang Y*, et al.* (2017) High-capacity, low-tortuosity, and channel-guided lithium metal anode. *Proc Natl Acad Sci U S A* 114(14):3584-3589.
22. Lin DC*, et al.* (2016) Layered reduced graphene oxide with nanoscale interlayer gaps as a stable host for lithium metal anodes. *Nature Nanotechnology* 11(7):626-632.

23. Liu Y*, et al.* (2016) Lithium-coated polymeric matrix as a minimum volume-change and dendrite-free lithium metal anode. *Nat Commun* 7:10992.
24. Li Y*, et al.* (2017) Revealing Nanoscale Passivation and Corrosion Mechanisms of Reactive Battery Materials in Gas Environments. *Nano Lett* 17(8):5171-5178.
25. Wood SM*, et al.* (2016) K+ Reduces Lithium Dendrite Growth by Forming a Thin, Less-Resistive Solid Electrolyte Interphase. *Acs Energy Letters* 1(2):414-419.
26. Hu Z*, et al.* (2017) Poly(ethyl α-cyanoacrylate)-Based Artificial Solid Electrolyte Interphase Layer for Enhanced Interface Stability of Li Metal Anodes. *Chem Mater* 29(11):4682-4689.
27. Lin D*, et al.* (2017) Conformal Lithium Fluoride Protection Layer on Three-Dimensional Lithium by Nonhazardous Gaseous Reagent Freon. *Nano Lett* 17(6):3731-3737.
28. Park K & Goodenough JB (2017) Dendrite-Suppressed Lithium Plating from a Liquid Electrolyte via Wetting of Li_3N. *Adv Energy Mater* 7(19):1700732.
29. Liang X*, et al.* (2017) A facile surface chemistry route to a stabilized lithium metal anode. *Nature Energy* 2(9):17119.
30. Cheng XB*, et al.* (2017) Nanodiamonds suppress the growth of lithium dendrites. *Nat Commun* 8(1):336.
31. Wang H, Lin D, Liu Y, Li Y, & Cui Y (2017) Ultrahigh–current density anodes with interconnected Li metal reservoir through overlithiation of mesoporous AlF_3 framework. *Science Advances* 3(9):e1701301.